Measuring image focusing for velocity analysis

Biondo Biondi

ABSTRACT

I present a method for extracting velocity information by measuring the focusing and unfocusing of migrated images. It measures image focusing by evaluating coherency across structural dips, in addition to coherency across aperture/azimuth angles. The inherent ambiguity between velocity and reflectors' curvature is directly tackled by introducing a curvature correction into the computation of the semblance functional that estimates image coherency. The resulting velocity estimator provides velocity estimates that are: 1) unbiased by reflectors' curvature, and 2) consistent with the velocity information that we routinely gather by measuring coherency over aperture/azimuth angles.

The application of the method to a 2D synthetic data set and a 2D field data set confirms that it provides consistent and unbiased velocity information. It also suggests that velocity estimates based on the new image-focusing semblance may be more robust and have higher resolution than estimates based on conventional semblance functionals. Preliminary tests on two 2D zero-offset synthetic data sets show that velocity information can be extracted from zero-offset data in presence of reflectors with arbitrary curvature, and not only in presence of point diffractors as previously published methods require.

INTRODUCTION

The effects of migration velocity on the focusing and unfocusing of seismic images is obvious when observing depth migrated seismic images obtained with different migration velocities. Quantitative measures of image focusing could provide valuable information to velocity estimation. This information is particularly abundant in areas where reflectors have strong curvature or are discontinuous; such as in presence of faults, heavily folded geology, buried channels, uncomformities or rough salt/sediment interfaces. Figure 1 shows three images obtained by migrating the same prestack data set: the top panel (a) shows the image obtained with too low migration velocity, the middle panel (b) shows the image obtained with approximately the correct velocity, and the bottom panel (c) shows the image obtained with too high velocity. An interpreter could easily spot clear signs of undermigration in Figure 1a and of overmigration in Figure 1c. However, the definition of objective quantitative criteria to measure image focusing is challenging. Consequently, current practical methods for exploiting image-focusing information are based on subjective interpretation criteria instead of quantitative measurements (Sava et al., 2005; Wang et al., 2006).

If we were able to extract reliably quantitative focusing-velocity information from migrated images it could supplement the velocity information that we routinely extract by analyzing residual moveout along offsets (after common-offset migration) or aperture-angles (after angle-domain migration) axes. Velocity estimation would be enhanced by increasing resolution and decreasing uncertainties. It would be particularly useful to improve the interpretability of the final image and the accuracy of time-to-depth conversion in areas where the reflection aperture range is narrow, either because of unfavorable depth/offset ratio, or because of the presence of high-velocity geological bodies in the overburden (e.g. salt bodies) that deflect the propagating waves. In practice, velocity analysis based on image focusing is unlikely to replace conventional velocity analysis, but only to supplement it. Therefore, a method that measures image focusing should provide velocity estimates that are consistent with conventional methods.

Figure 1 illustrates some of the challenges of defining quantitative criteria to measure image focusing. The main challenge is related to the ambiguity between reflectors' curvature and their apparent focusing velocity. The section migrated with approximately the correct velocity (Figure 1b) shows several convex reflectors with strong curvature. These reflectors collapse into high-amplitude foci in the overmigrated section (Figure 1c). Criteria that have been previously proposed to measure image focusing, such as maximization of the power of the stack or minimization of image entropy (Harlan et al., 1984; De Vries and Berkhout, 1984; Stinson et al., 2005; Fomel et al., 2007), would wrongly rank the overmigrated image higher than the more accurate image. When in the subsurface we have high-curvature reflectors, but not infinite curvature reflectors, the minimum-entropy criterion would fail because it assumes the presence of point scatterers in the subsurface.

Fomel et al. (2007) propose to separate in the data space the diffractions originated from point scatterers before performing minimum-entropy velocity analysis. However, in complex geology this separation can be unreliable, mostly because reflections from curved reflectors may appear as diffractions. This potential source of errors is also well illustrated by the field-data example. Figure 2 shows the near-offset section of the data set used to generate the images shown in Figure 1. The diffraction-like hyperbolic events visible in this section were generated by the high-curvature reflectors discussed above. An application aimed to separate diffractions from other events could easily classify these events for diffractions and lead to biased velocity estimates.

This paper aims to overcome the shortcomings of current methods used to measure image focusing. It presents a new method that has two important characteristics: 1) it is unbiased by reflectors' curvature, and 2) it provides velocity information from image focusing that is consistent with the velocity information that we routinely extract from migrated images by analyzing their coherency along the reflection-aperture angle axes. The method is based on the *image-focusing* semblance functional I introduced in Biondi (2008b), where I generalized the conventional semblance functional used to measure image coherency along the aperture-angle axes by defining an image-focusing semblance functional that simultaneously measures image coherency along

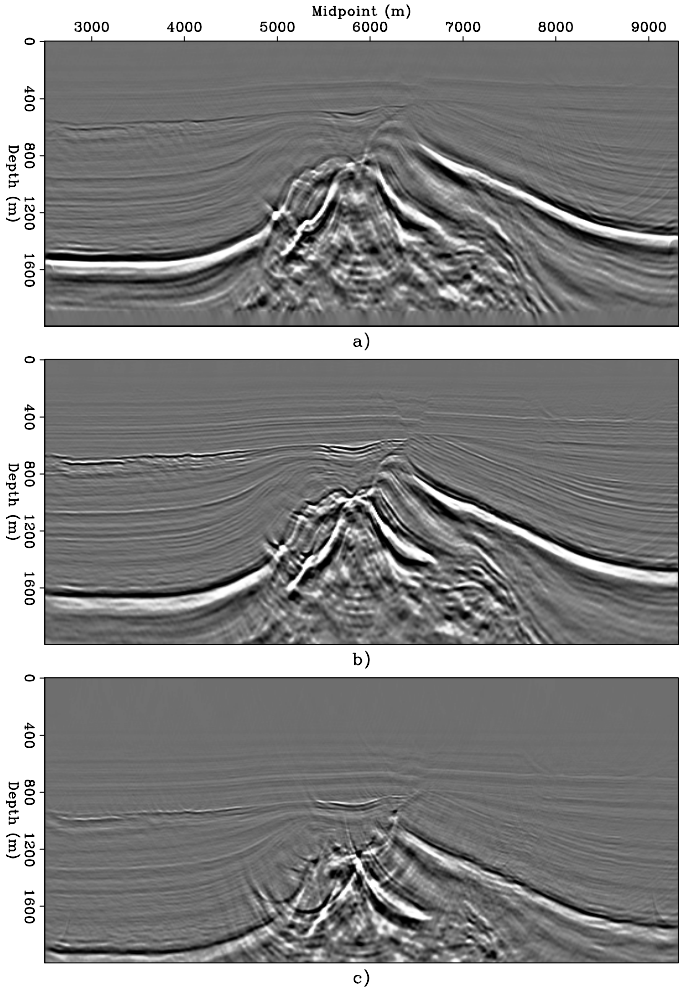

Figure 1: Three images obtained by prestack residual migration applied to the same prestack migration: the top panel (a) is undermigrated ($\rho = 0.8975$), the middle panel (b) s approximately well focused ($\rho = 1.01$), and the bottom panel (c) is overmigrated ($\rho = 1.2725$). [**CR**]

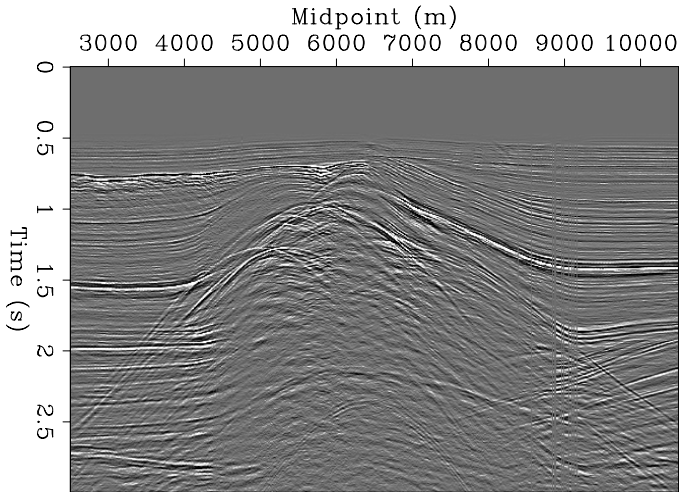

Figure 2: Near-offset section of the data set used to generate the images shown in Figure 1. [**CR**]

the structural-dip axes and the aperture-angle axes.

To remove the bias caused by reflectors' curvature, I explicitly take into account curvature by correcting its effects on image coherency along structural dips. Making curvature an explicit parameter of the velocity estimation does not necessarily resolves the fundamental problem of the ambiguity between the determination of reflectors' curvature and migration velocity. However, I show that it enables a consistent and unbiased velocity estimation that optimally uses the information contained in the data. In the last section of the paper, I present examples of image-focusing velocity analysis applied to two synthetic zero-offset data sets. These examples indicate that image-focusing analysis could automatically extract useful velocity information from zero-offset data even when the reflectivity model contains curved reflectors with finite curvature.

The simultaneous image-coherency measurement along both the structural-dip axes and the aperture-angle axes of the curvature-corrected images, assures the consistency of the velocity information provided by the method. This consistency facilitates the interpretation of the results. Furthermore, it may improve the robustness of velocity estimation with respect to conventional angle-domain methods by automatically averaging the coherency computation along reflectors. At each point on a reflector, image coherency is measured for several dips in addition to the stationary dip. The inclusion of non-stationary dips is equivalent to averaging coherency measurements along the reflector, following both its dip and its curvature.

In this paper, I present results of the proposed method applied to 2D data. The computation of the image-focusing semblance functional could be easily generalized from 2D to 3D. In 2D, semblance is computed on 2D patches (structural dip and aperture angle); with 3D full-azimuth data, semblance would be computed on 4D patches (indexed by two structural dips, reflection aperture and reflection azimuth). The curvature correction is also easily generalizable from 2D to 3D. However, three parameters are required to define curvature in 3D: the two main curvatures along the principal axes, and the rotation of the principal axes with respect to the coordinate axes (Al-Dossary and Marfurt, 2006). I expect the nature of the ambiguity between velocity and curvature to be different between 2D and 3D. In both cases velocity is defined by one scalar parameter, whereas curvature is defined by three parameters in 3D.

UNBIASED MEASURE OF IMAGE FOCUSING

In Biondi (2008b), I introduced a new semblance functional, that I dubbed *Image-focusing semblance*, aimed at quantitatively measuring image focusing simultaneously along the spatial directions and the reflection angle (or offset) axes. The underlying idea is to extend the conventional semblance evaluation by measuring image coherency also along the the structural-dip axes. However, the estimates provided by the image-focusing semblance presented in that report can be biased by reflectors'

curvature. In this section, I modify the definition of the image-focusing semblance by explicitly exposing its dependency from the image local curvature. This enables a consistent evaluation of the image focusing across both the reflection-angle axis and the structural-dip axis and improves the interpretability of the results.

The starting point of my method is an ensemble of prestack images, $\mathbf{R}(\mathbf{x},\gamma,\rho)$; these images are function of a spatial coordinate vector $\mathbf{x}=\{z,x\}$ (with z depth and x the horizontal location), the aperture angle γ, and a velocity parameter ρ. In the numerical examples that follow, the ensemble of prestack images is obtained by residual prestack migration in the angle domain as I presented in Biondi (2008a). The parameter ρ is the ratio between the new migration velocity and the migration velocity used for the initial migration. The proposed method could be easily adapted to the case when residual prestack Stolt migration (Sava, 2003), or any other method that can efficiently generate ensembles of prestack images dependent on a velocity parameter, is used to compute $\mathbf{R}(\mathbf{x},\gamma,\rho)$. Although, when using other methods to produce the ensemble $\mathbf{R}(\mathbf{x},\gamma,\rho)$, the corrections equivalent to equations 5, 8 and 9 might be different.

To measure coherency along the structural dip α, I first decompose the prestack image and create the dip-decomposed prestack image $\mathbf{R}(\mathbf{x},\gamma,\alpha,\rho)$. When using either choices of residual prestack migration discussed above, the decomposition can be efficiently performed in the Fourier domain during the residual prestack migration. If other methods are used to produce the ensemble of prestack images $\mathbf{R}(\mathbf{x},\gamma,\rho)$, the dip decomposition could as efficiently performed in the space domain by applying recursive filters (Fomel, 2002; Hale, 2007). Notice, that the dip-decomposed images I use as input have different kinematic characteristics than the ones described in Reshef and Rüger (2008), Landa et al. (2008), and Reshef (2008). They obtain dip-decomposed images by not performing the implicit summation over dips that is part of angle-domain Kirchoff migration (Audebert et al., 2002), whereas I decompose the migrated images.

In equation 5 in Biondi (2008b) I defined the 2D Image-focusing semblance as:

$$S_{(\gamma,\alpha)}(\mathbf{x},\rho)=\frac{\left[\sum_{\gamma}\sum_{\alpha}\mathbf{R}(\mathbf{x},\gamma,\alpha,\rho)\right]^2}{N_{\gamma}N_{\alpha}\sum_{\gamma}\sum_{\alpha}\mathbf{R}(\mathbf{x},\gamma,\alpha,\rho)^2}, \tag{1}$$

where N_{γ} and N_{α} are, respectively, the number of aperture angles and the number of dips to be included in the computation. The effective definition of the aperture-angle and the structural-dip ranges to be used in equation 1 is one of the practical challenges when applying the proposed method.

Image curvature and residual migration

In presence of point diffractors, the semblance functional defined in expression 1 yields unbiased estimates of the velocity parameter ρ. However, when the curvature is finite,

the dip components would not be aligned for the correct value of ρ and the estimates would be biased. To remove this bias we can correct the dip-decomposed images for the presence of curvature. In Appendix A I show the simple derivation of this correction that amounts to the following spatial shift, $\Delta\mathbf{n}_{\text{Curv}}$, along the normal to the structural dip,

$$\Delta\mathbf{n}_{\text{Curv}} = \frac{\sin(\alpha-\bar{\alpha})\tan(\alpha-\bar{\alpha})}{2} R\mathbf{n}, \tag{2}$$

where R is the local radius of curvature, $\bar{\alpha}$ is the local dip and $\mathbf{n}$ is the vector normal to the dip α and directed towards increasing depth. Notice that the application of this correction requires the estimation of local dip $\bar{\alpha}$. To estimate the local dips, I used the Seplib program *Sdip* that implements a variant of the algorithms described by Fomel (2002).

Expression 2 can be used directly to create an ensemble to dip-decomposed images that are corrected for the local curvature $\mathbf{R}_{\text{Curv}}(\mathbf{x},\gamma,\alpha,\rho,R)$. The image-focusing semblance can be computed on these images as:

$$S_{(\gamma,\alpha)}(\mathbf{x},\rho,R) = \frac{\left[\sum_\gamma \sum_\alpha \mathbf{R}_{\text{Curv}}(\mathbf{x},\gamma,\alpha,\rho,R)\right]^2}{N_\gamma N_\alpha \sum_\gamma \sum_\alpha \mathbf{R}_{\text{Curv}}(\mathbf{x},\gamma,\alpha,\rho,R)^2}. \tag{3}$$

However, the application of correction 2 can be quite expensive unless it is performed together with residual migration. Furthermore, precomputing the curvature-corrected images would further increase the dimensionality of the image space, creating obvious problems for handling the resulting bulky data sets. Fortunately, when the ensemble of the dip-decomposed images $\mathbf{R}(\mathbf{x},\gamma,\alpha,\rho)$ are the result of residual prestack migration, the curvature correction can be efficiently computed during the evaluation of the semblance functional 3. Correction 2 becomes a simple interpolation along the residual velocity parameter ρ, as a function of the aperture angles and dips.

To derive the interpolating function, I first recall the expression of residual migration in Biondi (2008a):

$$\Delta\mathbf{n}_{\text{Rmig}} = (\rho_{\text{new}} - \rho_{\text{old}}) \frac{\cos\alpha}{\left(cos^2\alpha - \sin^2\gamma\right)} z_0\mathbf{n}, \tag{4}$$

where $\Delta\mathbf{n}_{\text{Rmig}}$ is the normal shift applied by residual migration, ρ_{new} is the value of ρ after residual migration and ρ_{old} is the value of ρ before residual migration, which is usually set to be equal to one. The parameter z_0 is a constant that is equal to the depth for which the residual migration in 4 is exact.

Equating the normal shift in 4 with the normal shift in 2 and solving for ρ_{new} we obtain

$$\rho_{\text{new}} = \rho_{\text{old}} + \frac{\sin(\alpha-\bar{\alpha})\tan(\alpha-\bar{\alpha})\left(\cos^2\alpha - \sin^2\gamma\right)}{2\cos\alpha z_0} R. \tag{5}$$

In this case, ρ_{new} is the ρ of the images from which the data are interpolated from, and ρ_{old} is the ρ of the images after correction; that is,

$$\mathbf{R}_{\text{Curv}}(\mathbf{x},\gamma,\alpha,\rho_{\text{old}},R) = \mathbf{R}\left[\mathbf{x},\gamma,\alpha,\rho_{\text{new}}(\rho_{\text{old}},\gamma,\alpha,\bar{\alpha},R)\right]. \tag{6}$$

Image curvature and residual migration in the pseudo-depth domain

The interpolation defined by 5 depends in a non-straightforward manner from both angles γ and α, as well as from the estimate of the local dip $\bar{\alpha}$. Although, this is the relationship I used in practice for the examples in this paper, I will now analyze one of its variants that is simpler and thus it helps to better understand the relationship between image curvature and residual migration parameter.

I start from redefining residual migration in the pseudo-depth domain $\tilde{z} = z/\rho$ (Sava, 2004). In this domain, the focusing/unfocusing effects of residual migration are better separated from its mapping effects than in the conventional depth domain. In the pseudo-depth domain, normal-incidence images of flat reflectors are not shifted by residual migration. The expression of residual migration 4 becomes:

$$\Delta \mathbf{n}_{\text{Rmig}} = (\rho_{\text{new}} - \rho_{\text{old}}) \left[\frac{\cos\alpha}{\left(\cos^2\alpha - \sin^2\gamma\right)} - \cos\alpha \right] z_0 \mathbf{n}, \tag{7}$$

and the expression of curvature correction 5 becomes:

$$\rho_{\text{new}} = \rho_{\text{old}} + \frac{\sin^2(\alpha - \bar{\alpha}) \left(\cos^2\alpha - \sin^2\gamma\right)}{2 z_0 \cos(\alpha - \bar{\alpha}) \cos\alpha \left(\sin^2\alpha + \sin^2\gamma\right)} R, \tag{8}$$

that also does not provide a straightforward relationship between the input and output ρs. Furthermore, it becomes singular for the flat dip component ($\alpha = 0$) of normal incidence images ($\gamma = 0$). Its use is thus more cumbersome than the use the equivalent expression in the depth domain (equation 5).

However, in the special case of events that are locally flat ($\bar{\alpha} = 0$) and are imaged at normal-incidence (i.e. $\gamma = 0$), this expression simplifies into:

$$\rho_{\text{new}} = \rho_{\text{old}} + \frac{R}{2 z_0}. \tag{9}$$

In this case, the curvature correction becomes independent from the dip α. It only remaps the image from ρ_{new} to ρ_{old} and thus does not affect the coherency along the dip direction of the dip-decomposed images. There is perfect ambiguity between the residual migration parameter ρ and the reflector radius of curvature R.

SYNTHETIC-DATA EXAMPLE

To illustrate the proposed method, I first present its application to a synthetic data set. The model is a medium with constant slowness of .5 s/km and a single reflector with sinusoidal shape. This reflector is shown in Figure 3. I modeled a prestack data set with offsets between -1.5 kilometers and 1.5 kilometers. I then migrated the data

with both the correct slowness and a high slowness of .525 s/km; that is, 105% the correct slowness.

I dip-decomposed the image obtained with the correct slowness at zero-subsurface offset and corrected it for curvature according to expression 5. Figure 4a shows the dip-decomposed image at the midpoint of one of the bottoms of the sinusoid (x=4.250 km). Because of the curvature, the dips are not aligned and the event is frowning down. Figure 4b shows the panel in Figure 4a corrected for image curvature by applying the shift defined in expression 2. I selected the radius of curvature to be equal to -90 meters. This is consistent with the analytical radius of curvature of the sinusoidal reflector at the same location of -86 meters. I set the reflector local dip to be zero; that is, I set $\bar{\alpha} = 0$ in expression 2.

The panels shown in Figure 5 are equivalent to the panels shown in Figure 4, except that the midpoint location is at one of the tops of the sinusoid (x=4.750 km). At this location the curvature is positive and thus the uncorrected dip panel (Figure 5a) smiles upward. The corrected panel (Figure 5b) corresponds to a positive radius of curvature of 90 meters.

I computed the conventional semblance over aperture angle and the proposed image-focusing semblance from the migrated image obtained with the high slowness. Figure 6 compares the semblance fields computed by the conventional semblance functional that measures coherency only over aperture angles (Figure 6a), with the semblance cube computed by the proposed image-focusing semblance functional that measures coherency over both aperture angles and structural dips (Figure 6b). The figure shows the semblance fields at x=4.750 km, that is at one of the local top of the sinusoidal reflector. The ρ-range is the same ($0.984 \leq \rho \leq 1.134$) for the two panels in the figure. The semblance peak is more sharply defined as a function of the ρ parameter in the result of the new image-focusing functional (right face in Figure 6b) than in the result of conventional method (Figure 6a).

Notice that the semblance peak is located at longer radius of curvature (R=125 meters) than the actual radius of curvature of the reflector (R=86 meters), because residual migration in the angle domain is not exact and does not fully correct for the reflector curvature. This error is inconsequential for the proposed method since the aim is to better estimate ρ not R.

FIELD-DATA EXAMPLE

I applied the proposed method to a 2D marine line extracted from a 3D data set. The images shown in Figure 1 were produced from this 2D line. I will focus on the analysis of the results for a small window of the image that contains both convex and concave reflectors. In contrast with the previous synthetic-data example, I performed the curvature correction defined in equation 5 by using a field of local dips estimated numerically. I applied the Seplib program *Sdip* to the ensemble of sections obtained by stacking along the aperture-angle axis the residual migrated images for each value

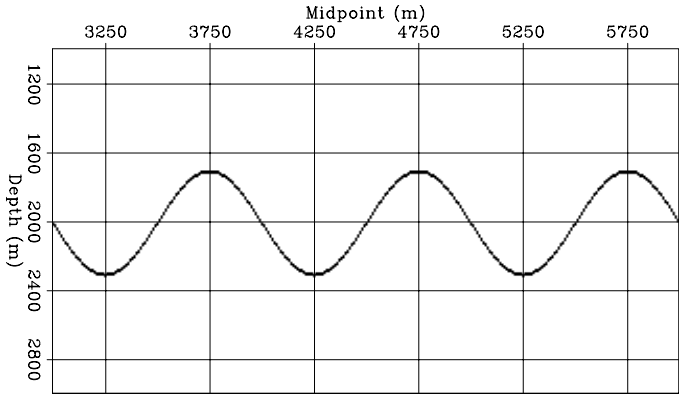

Figure 3: Sinusoidal reflector used to generate the synthetic prestack data set. [**ER**]

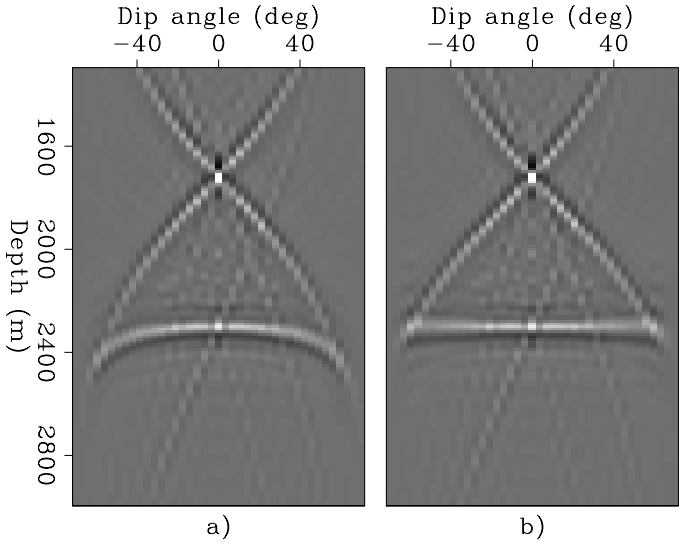

Figure 4: The dip-decomposed images at the midpoint of one of the bottoms of the sinusoidal reflector (x=4.250 km): without curvature correction (panel a) and after curvature correction (panel b). [**CR**]

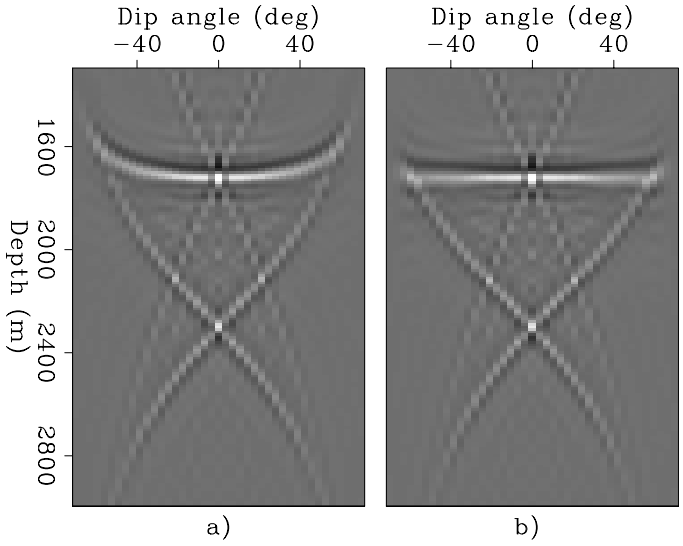

Figure 5: The dip-decomposed images at the midpoint of one of the tops of the sinusoidal reflector (x=4.750 km): without curvature correction (panel a) and after curvature correction (panel b). [**CR**]

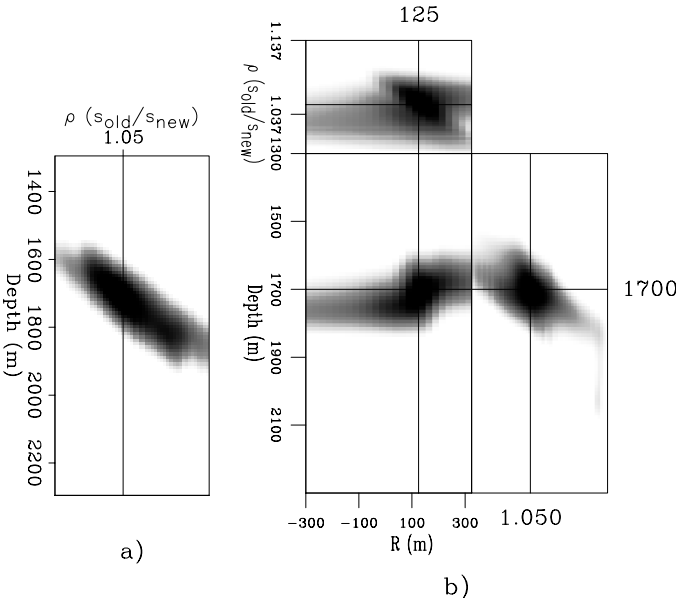

Figure 6: Comparison of the semblance fields computed by the conventional semblance functional that measures coherency only over aperture angles (panel a), with the semblance cube computed by the proposed image-focusing semblance functional that measures coherency over both aperture angles and structural dips (panel b). The figure shows the semblance fields at x=4.750 km. [**CR**]

of ρ.

Figure 7a shows the migrated stack of the analysis window for a particular choice of the ρ parameter (ρ=1.04) that maximizes flatness in the aperture-angle gather at the midpoint location corresponding to the black line superimposed onto the stack; that is for x=5.646 km. Figure 7b shows the aperture-angle gather and Figure 7c the corresponding semblance panel.

Starting from the prestack images, I computed dip-decomposed images that are function of both the aperture angle γ and the structural dip α. Figure 8 shows the 3D cube of the dip-decomposed image at the same midpoint location as the previous figure; that is for x=5.646 kilometers. The convex reflector of interest, at depth of 950 meters, shows an upward-smiling moveout in the structural-dips panel, consistently with the result observed when discussing the synthetic-data example in the previous section. Figure 9 displays the image-focusing semblance cube at that same midpoint location. The left panel in the cube displays semblance as a function of depth and radius of curvature (R) at ρ=1.04; the right panel displays semblance as a function of depth and ρ at R=125 meters. The location of the semblance peak in the cube at depth of 950 meters is consistent with the location of the semblance peak in the conventional ρ scan shown in Figure 7c. The semblance peak in the image-focusing cube is slightly tighter than in the conventional scan, but the differences are not substantial.

Figures 10-12 shows similar analysis of the migrated images presented above, but at the midpoint location corresponding to the reflector with negative curvature; that is for x=5.539 kilometers. The reflector is locally dipping with negative dip of approximately 45 degrees. The stationary point in the dip-decomposed image shown in the right panel of Figure 11 is located at that value of the structural dip, and it is frowning instead of smiling because of the negative local curvature. The value of ρ for

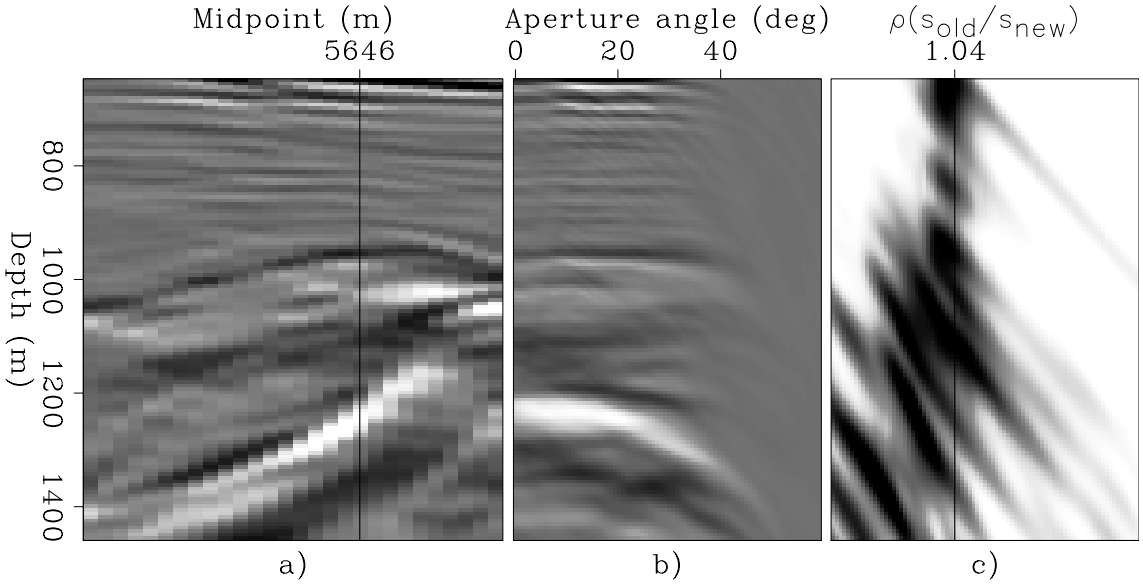

Figure 7: The migrated stack of the analysis window for ρ=1.04 (panel a), the aperture-angle gather at x=5.5646 km for ρ=1.04 (panel b), and the aperture-angle semblance section at x=5.646 km (panel c). [**CR**]

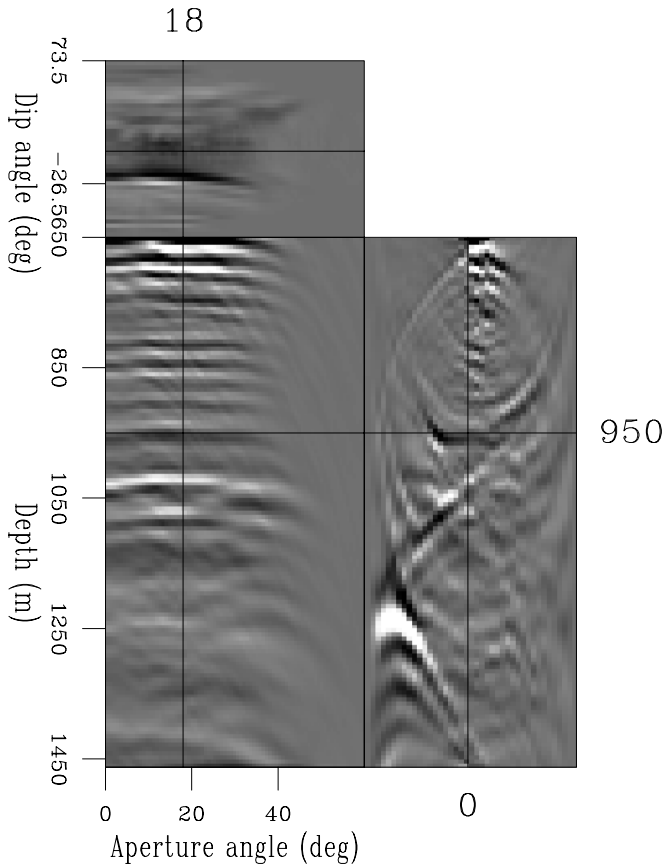

Figure 8: The dip-decomposed image at x=5.646 kilometers. The convex reflector of interest, at depth of 950 meters, shows an upward-smiling moveout in the structural-dips panel. [**CR**]

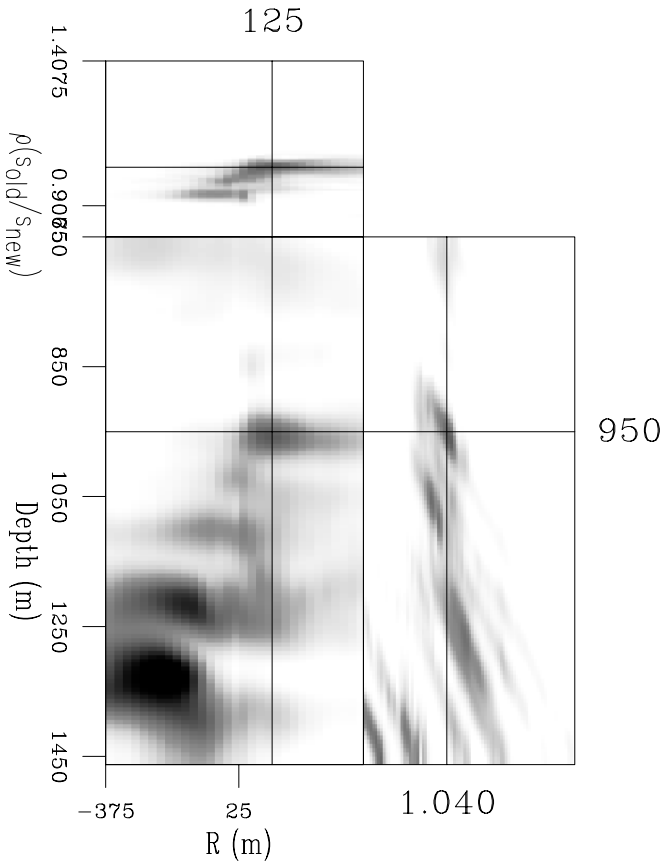

Figure 9: The image-focusing semblance cube at x=5.646 kilometers. The location of the semblance peak in the cube at depth of 950 meters is consistent with the location in the conventional ρ scan shown in Figure 7c. The peak is slightly tighter than in the conventional scan. [**CR**]

which the reflector is the flattest along the aperture-angle axis (ρ=.95), is substantially lower than for the previous reflector (ρ=1.04). This substantial difference in apparent velocity, notwithstanding the proximity of the two midpoint locations, is probably related to the fact that the wavefronts that illuminate the two events propagate through different zones of the velocity model due to the dip of the second reflector.

The semblance peak in the image-focusing cube (right panel in Figure 12) is now substantially better defined than in the conventional semblance panel shown in Figure 10c, suggesting a potential resolution benefit for velocity estimation. Further analysis of this potential benefit is needed before drawing definitive conclusions.

Another potential advantage of explicitly taking into account, and correcting for, reflectors' curvature in the semblance analysis, is that it automatically enables the simultaneous measurements of coherency for several structural dips, in addition to the stationary dip, at each analysis point. The semblance measurements are thus automatically averaged along the reflector, following both its local dip and its local curvature. To test this hypothesis, I computed a modified version of the conventional semblance functional along the aperture-angle axis according to the following expression:

$$S_\gamma\left(\mathbf{x},\rho,R\right)=\frac{\sum_\alpha\left[\sum_\gamma \mathbf{R}_{\text{Curv}}\left(\mathbf{x},\gamma,\alpha,\rho,R\right)\right]^2}{\sum_\alpha N_\gamma \sum_\gamma \mathbf{R}_{\text{Curv}}\left(\mathbf{x},\gamma,\alpha,\rho,R\right)^2}, \tag{10}$$

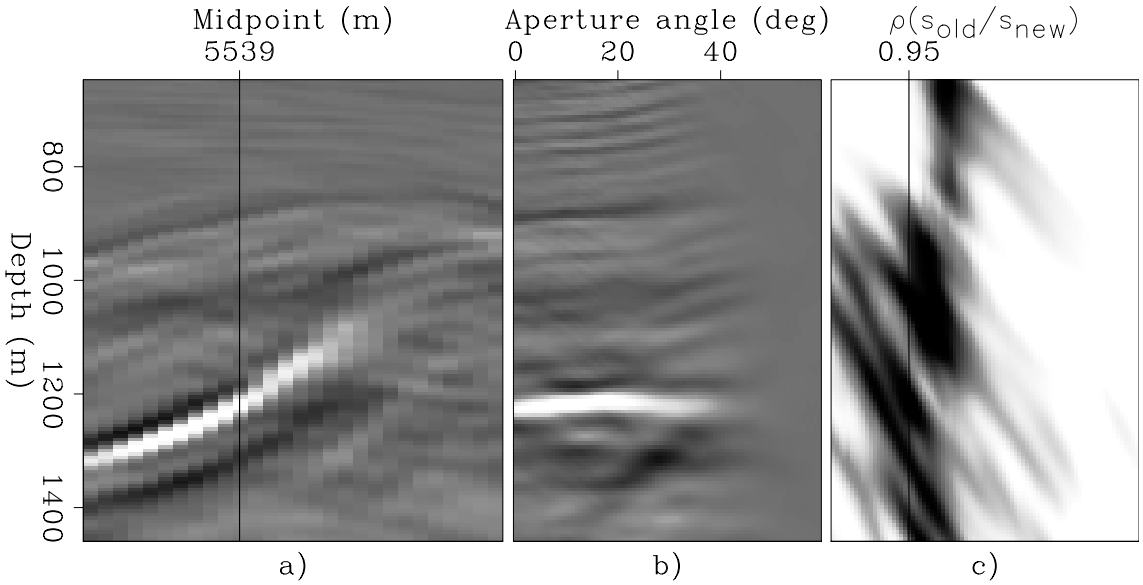

Figure 10: The migrated stack of the analysis window for ρ=0.95 (panel a), the aperture-angle gather at x=5.539 km for ρ=0.95 (panel b), and the aperture-angle semblance section at x=5.539 km (panel c). [**CR**]

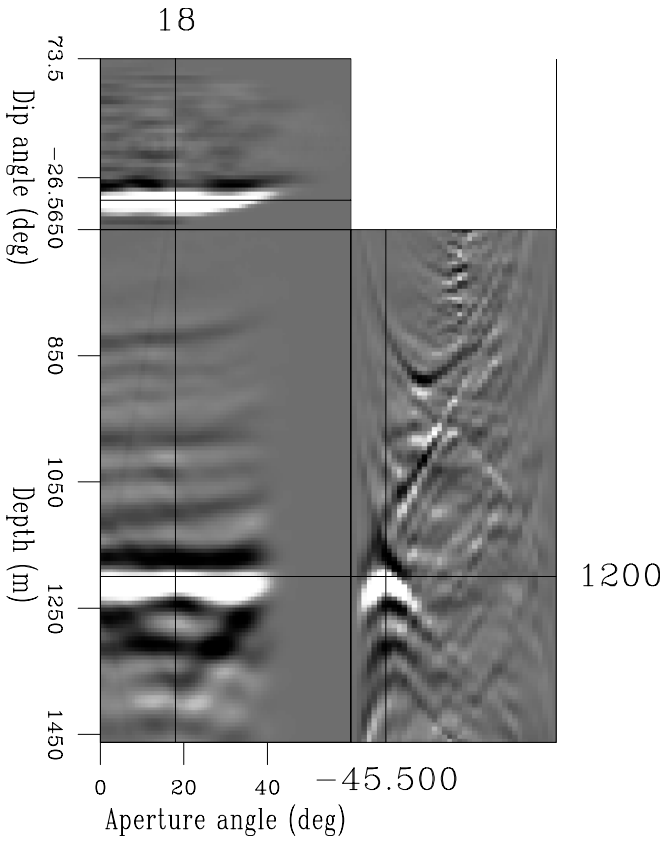

Figure 11: The dip-decomposed image at x=5.539 kilometers. The concave reflector of interest, at depth of 1200 meters and dip of 45 degrees, shows a downward-frowning moveout in the structural-dips panel. [**CR**]

that averages both numerator and denominator along the structural-dip axis. Figure 13 compares the result of conventional semblance with the result of computing the semblance functional defined in 10. Figure 13c displays conventional semblance, and it is the same panel shown in Figure 10c. Figure 13a displays the constant ρ section of the semblance cube computed using 10 and Figure 13b displays the constant curvature (R=-75 meters) section of this semblance cube. Although both panel b) and panel c) are computed by measuring coherency only along the aperture-angle axis, the semblance peak corresponding to the concave reflector is clearly better focused and more easily pickable in panel b) than in panel c). This example suggests that there is an advantage on averaging semblance over structural dips. On the other hand, there is the additional cost of computing the dip-decomposed images and the additional complexity of picking a higher dimensionality semblance cube.

ZERO-OFFSET SYNTHETIC-DATA EXAMPLE

The synthetic-data and field-data examples discussed in the two previous sections applied the image-focusing semblance to prestack data sets, where useful velocity information is provided by the data redundancy over offsets. In this section, I present experiments on two simple zero-offset synthetic data sets. The only velocity information contained in the migrated images obtained from zero-offset data is the focusing and unfocusing of reflections.

Figure 14 shows the reflectors' geometry assumed to model the two synthetic data sets. I modeled the first data set assuming a "cloud" of point diffractors (panel a), whereas I modeled the second data set assuming a "cloud" of convex reflectors (panel b). In both cases the velocity was assumed to be constant and equal to 2 km/s and the data were migrated assuming a high slowness of .5125 s/km; that is, 102.5% of the correct slowness.

Figure 15 summarizes the main result of this section. All three panels show the image-focusing semblance spatially averaged in an inner rectangle of the image space defined by the following inequalities along the depth axis: 1.850 km $\leq$ z $\leq$ 2.150 km, and by the following inequalities along the midpoint axis: 4.875 km $\leq$x$\leq$ 5.125 km. The panel shows the average semblance as a function of the velocity parameter ρ and the radius of curvature R. Figure 15a shows the result corresponding to the point diffractors and Figure 15b shows the result corresponding to the convex reflectors. In both cases, I applied the curvature correction defined in 5 by using a field of local dips ($\bar{\alpha}$) estimated numerically by applying the Seplib program *Sdip* to the ensemble of residual migrated images for each value of ρ.

The important observation supported by this figure is that, in both Figure 15a and Figure 15b, the semblance energy is concentrated in a relatively narrow interval that includes the correct value of ρ; that is $\rho = 1.025$. This result indicates that we can extract useful velocity information from zero-offset data by using the image-focusing semblance.

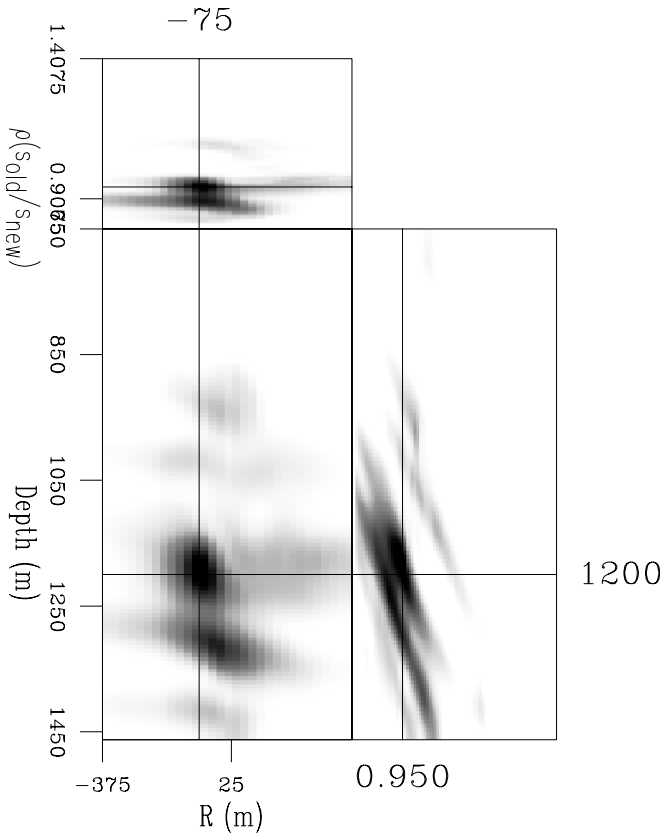

Figure 12: The image-focusing semblance cube at x=5.539 kilometers. The location of the semblance peak in the cube at depth of 1200 meters is consistent with the location in the conventional ρ scan shown in Figure 10c, but is substantially better defined than in the conventional scan. [**CR**]

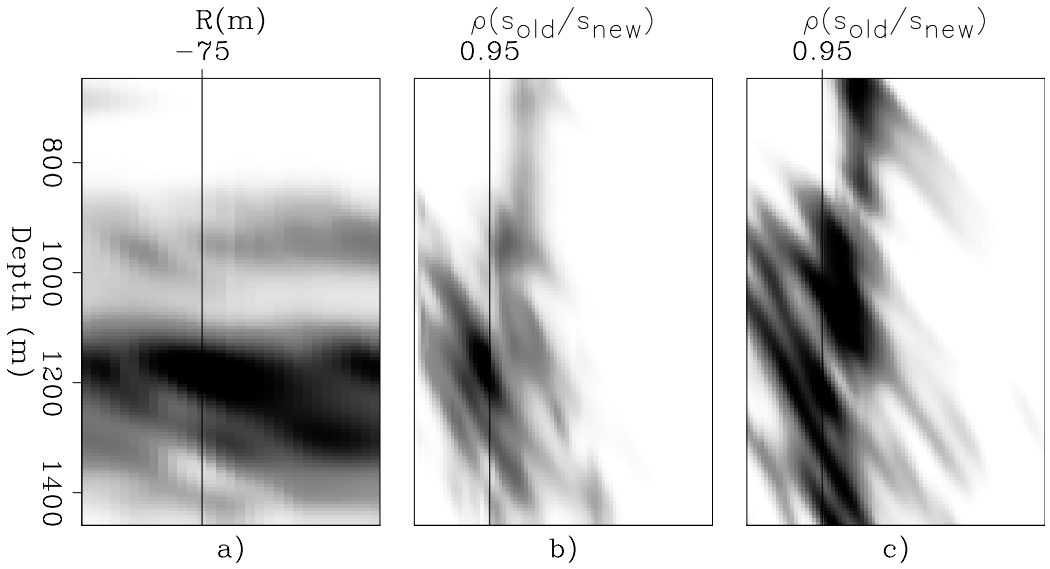

Figure 13: Comparison of the result of computing the semblance functional defined in 10 (panels a and b) with the result of conventional semblance (panel a), at x=5.539 kilometers. The semblance peak corresponding to the concave reflector is clearly better focused and more easily pickable in panel b) than in panel c). [**CR**]

The third panel in Figure 15, shows the semblance average computed from the images of the convex reflectors when I applied the curvature correction defined in 5 by using a constant local dip equal to zero; that is, when I uniformly set $\bar{\alpha} = 0$. As predicted by expression 9, there is strong ambiguity between the reflector curvature and the velocity parameter and the semblance is high also for values of ρ that are far away from the correct one. We can consequently conclude that the velocity information contained in panel a) and b) derives from the inconsistency between the focusing information extracted using the image-focusing semblance and the local dip estimation. This inconsistency occurs when the image is sufficiently unfocused that the local dip estimation becomes unreliable. The following figures illustrate this concept.

Figures 16–20 provide a graphical explanation of the results shown in Figure 15. Figure 16 shows the migrated images of the point-diffractors data corresponding to the values of ρ at the edges of the semblance peak in Figure 15a. The inner rectangle delimited by the grid superimposed to the images shows where the semblance is spatially averaged to produce the results shown in Figure 15. The image in Figure 16a is undermigrated and corresponds to $\rho = 1.0125$, whereas the image in Figure 16b is overmigrated and corresponds to $\rho = 1.0375$. In both of these images the unfocusing starts to cause crossing of events in the inner rectangle delimited by the grid superimposed to the images. The local dips are then multivalued and the automatic estimation of the local dips becomes unreliable and inconsistent with the more global behavior of the dips. Therefore, outside the interval $1.0125 \leq \rho \leq 1.0375$ the semblance average drops substantially in value.

Similar behavior is displayed by the migrated images of the convex-reflectors data corresponding to the values of ρ at the edges of the semblance peak in Figure 15a. These images are shown in Figure 17, and correspond to $\rho = 1.01$ (Figure 17a), and to $\rho = 1.07$ (Figure 17b). In this case, the ρ range is wider than in the previous case because the convex-reflectors' density is lower than the point-diffractors' density, and thus a larger velocity error is needed before poorly focused events start crossing.

Figures 18–20 show sections cut through the image-focusing semblance cubes at constant value of ρ and R before spatial averaging. Figure 18a shows semblance for the point-diffractors data for $\rho = 1.025$ and $R = 0$ meters; that is, the values of ρ and R for which the data are best focused. Figure 18a shows semblance for $\rho = 1.0125$ and $R = 40$ meters. This value of ρ is the one corresponding to the undermigrated image in Figure 16a. Because of undermigration, the image from the point diffractors appears to have a positive radius of curvature approximately equal to 40 m. However, because of inconsistency between the focusing information and the local dip estimation, semblance is in average lower in the panel on the right than in the panel on the left.

Similar behavior is displayed by the image-focusing semblance cubes computed from the images of the convex-reflectors data. We find the "best focused" semblance panel (Figure 19a) still at infinite curvature ($R = 0$ meters), but at a wrong value of ρ; that is, at $\rho = 1.04$. However, the important result is that the interval with relative high semblance still includes the correct value of ρ. The section shown in

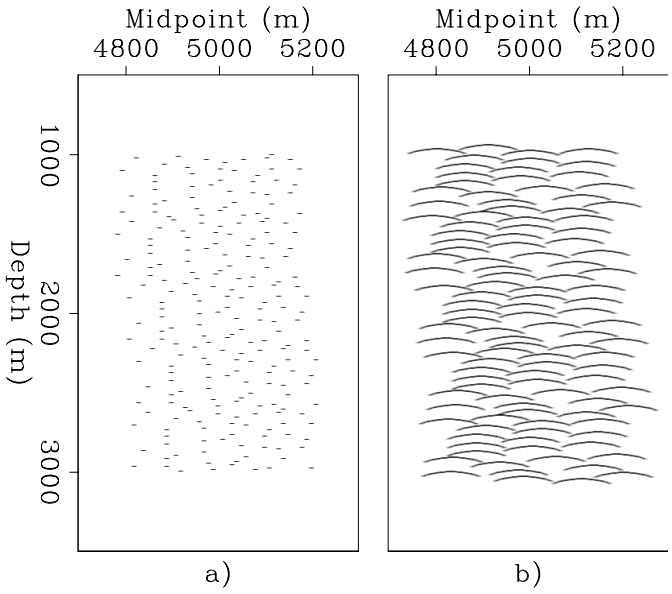

Figure 14: Reflectors' geometry assumed to model the two zero-offset synthetic data sets I used to test the proposed image-focusing velocity-estimation method: a) a "cloud" of point diffractors, and b) a "cloud" of convex reflectors. [**ER**]

Figure 19b corresponds to undermigrated image shown in Figure 19b, and it is taken for $\rho = 1.01$ and $R = 120$ meters. The apparent curvature is lower than for the point diffractors because the actual curvature of the reflector is lower.

Finally, Figure 20 shows sections through the image-focusing semblance cubes for the convex-reflectors data when the local dip is uniformly set equal to zero. These panels correspond to the average semblance shown in Figure 15c, and are sections taken for the same values of ρ and R as the sections shown in Figure 17. Because of the ambiguity between velocity and curvature, both panels show well-focused and high value semblance peaks.

DISCUSSION AND CONCLUSIONS

Using image focusing and unfocusing for velocity estimation has been for long time an elusive goal in reflection seismology. The main challenge is the ambiguity between image focusing and reflectors' curvature. Consequently, previously published methods had to rely on strong assumptions on reflectors' curvature, such as assuming that reflections were generated by point diffractors; that is, by infinite-curvature reflectors. I present a method that does not rely on this assumption because it explicitly takes into account of reflectors' curvature when measuring image focusing.

The synthetic-data example I present in the third section and the field-data example I present in the fourth section show that the method may provide higher resolution and more robust velocity information than conventional methods based on measuring image coherency only along the aperture-angle axes (or the offset axes when constant-offset migration is performed.) Furthermore, the proposed method extract image-focusing information from prestack data that is consistent with the velocity information that we routinely extract by measuring image coherency along

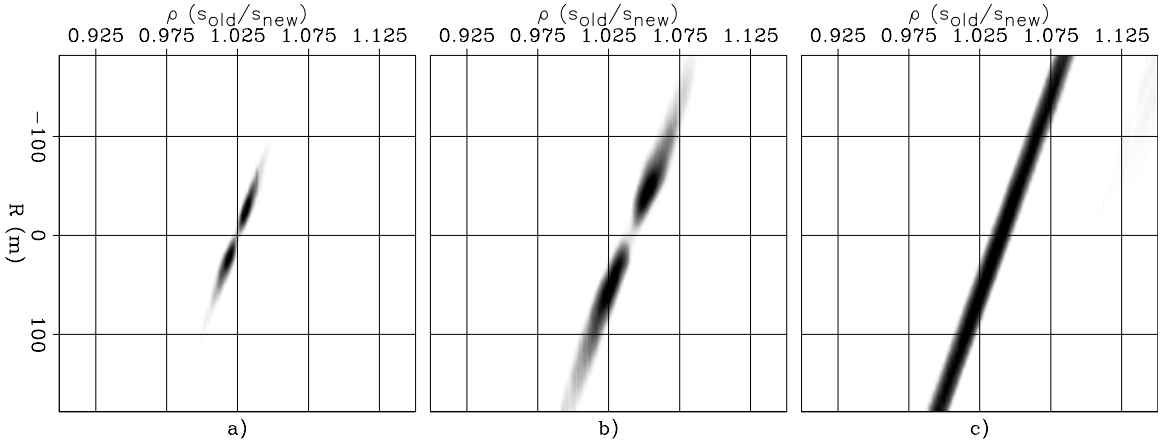

Figure 15: The image-focusing semblance spatially averaged in an inner rectangle of the image space as a function of velocity parameter ρ and the radius of curvature R. Panel a) shows the result corresponding to the point diffractors, and panel b) shows the result corresponding to the convex reflectors when the curvature correction was applied by using a field of local dips estimated numerically from the migrated images. Panel c) shows the result corresponding to the convex reflectors when the curvature correction was applied by using a constant local dip equal to zero (i.e. $\bar{\alpha} = 0$). [**CR**]

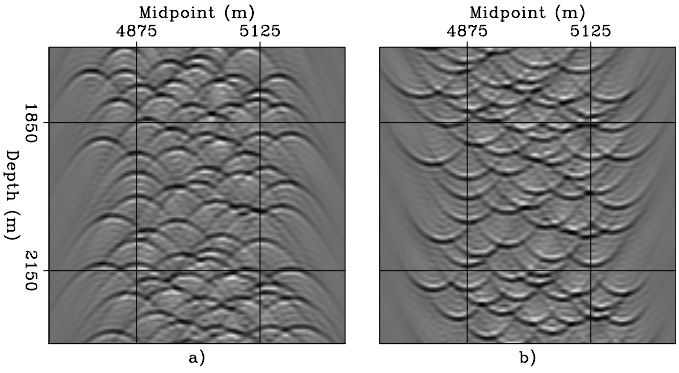

Figure 16: Migrated images of the point-diffractors data corresponding to the values of ρ at the edges of the semblance peak in Figure 15a; that is, $\rho = 1.0125$ for panel a), and $\rho = 1.0375$ for panel b). [**CR**]

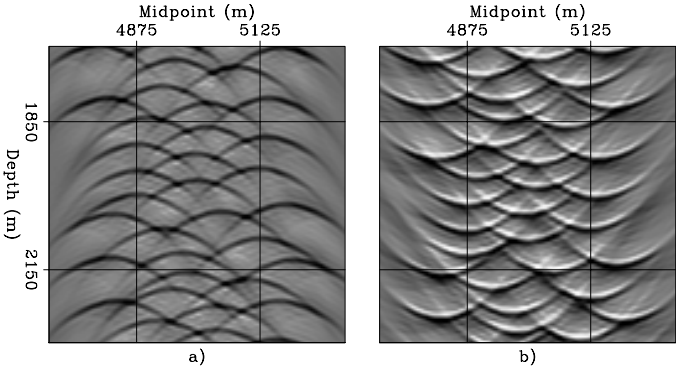

Figure 17: Migrated images of the convex-reflectors data corresponding to the values of ρ at the edges of the semblance peak in Figure 15b; that is, $\rho = 1.01$ for panel a), and $\rho = 1.7$ for panel b). [**CR**]

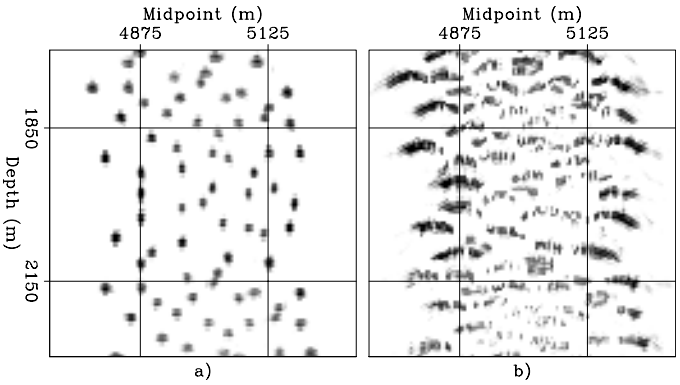

Figure 18: Sections cut through the image-focusing semblance cubes at constant value of ρ and R before spatial averaging. These panels were computed from the point-diffractors data. Panel a) shows semblance for $\rho = 1.025$ and $R = 0$ meters, and panel b) shows semblance for for $\rho = 1.0125$ and $R = 40$ meters. [**CR**]

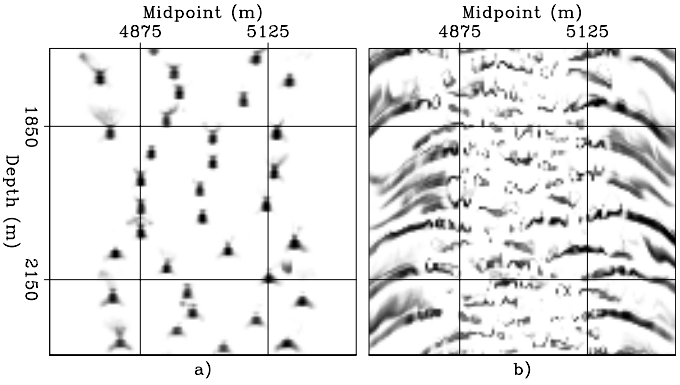

Figure 19: Sections cut through the image-focusing semblance cubes at constant value of ρ and R before spatial averaging. These panels were computed from the convex-reflectors data. Panel a) shows semblance for $\rho = 1.04$ and $R = 0$ meters, and panel b) shows semblance for for $\rho = 1.01$ and $R = 120$ meters. [**CR**]

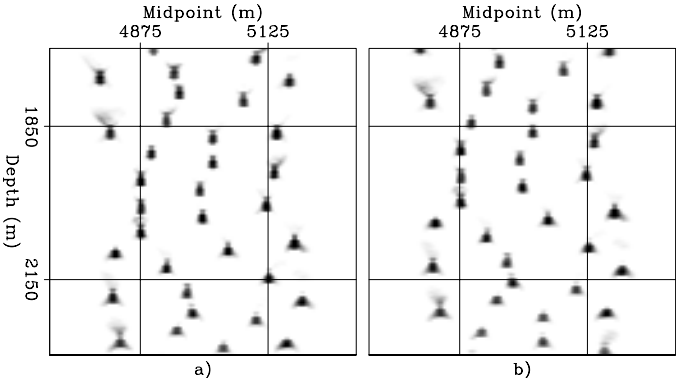

Figure 20: Sections cut through the image-focusing semblance cubes at constant value of ρ and R before spatial averaging. These panels were computed from the convex-reflectors data. The local dip was set to be constant and equal to zero when applying the curvature correction. In contrast, the local dips were numerically estimated when computing the semblance panels shown in Figure 19. Panel a) shows semblance for $\rho = 1.04$ and $R = 0$ meters, and panel b) shows semblance for for $\rho = 1.01$ and $R = 120$ meters. [**CR**]

the aperture-angle axes.

The two zero-offset synthetic-data examples I show in the last section suggest that useful velocity information can be extracted from zero-offset data. Images that were migrated with approximately the correct velocity have no crossing events and thus the local dip information measured from these images is consistent with the focusing information measured by the image-focusing semblance functional. When the migration velocity is far from the correct one, the migrated images have a lot of crossing events. The local-dips information measured from these images is unreliable and inconsistent with the focusing information measured by the image-focusing semblance functional. These results suggest that it might be useful to estimate the reflectors' curvature by local curvature estimators (Al-Dossary and Marfurt, 2006) and use this information to further constrain the velocity estimates obtained by applying the image-focusing semblance proposed in this paper.

APPENDIX A

CURVATURE CORRECTION

This appendix derives the expression for the curvature correction presented in the main text in 2. The derivation is extremely simple and based on the geometry sketched in Figure 21.

The reflector is approximated with a parabola with radius of curvature R at its vertex. In the rotated coordinates system (z', x') the equation of the parabola is

$$z' = \frac{x'^2}{2R}. \tag{A-1}$$

The shift $\Delta z'$ that moves a tangent to the parabola to the vertex is equal to

$$\Delta z' = \tan^2 \alpha' \frac{R}{2}, \tag{A-2}$$

and consequently the normal shift Δn is equal to

$$\Delta n = \frac{\cos \alpha' \tan^2 \alpha'}{2} R = \frac{\sin \alpha' \tan \alpha'}{2} R. \tag{A-3}$$

The coordinate system (z', x') is rotated by $\bar{\alpha}$ with respect to (z, x). Removing that rotation is equivalent to set $\alpha' = \alpha - \bar{\alpha}$; performing this substitution in the previous equation, I obtain the correction in 2; that is,

$$\Delta n = \frac{\sin (\alpha - \bar{\alpha}) \tan (\alpha - \bar{\alpha})}{2} R. \tag{A-4}$$

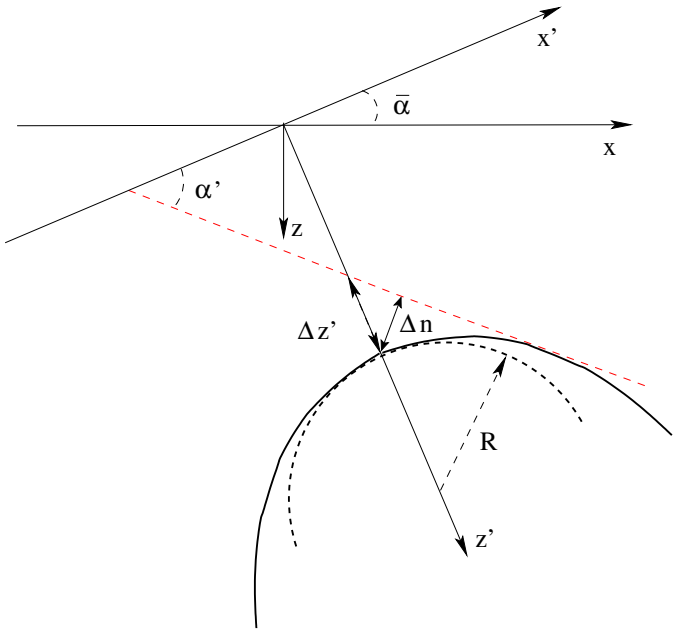

Figure 21: Sketch used to derive the curvature correction presented in 2. The tangent to the parabola (dashed line) needs to be shifted by Δn to pass through the vertex of the parabola. [**NR**]

REFERENCES

Al-Dossary, S. and K. J. Marfurt, 2006, 3d volumetric multispectral estimates of reflector curvature and rotation: Geophysics, **71**, P41–P51.

Audebert, F., P. Froidevaux, H. Rakotoarisoa, and J. Svay-Lucas, 2002, Insights into migration in the angle domain: SEG Technical Program Expanded Abstracts, **21**, 1188–1191.

Biondi, B., 2008a, Automatic wave-equation migration velocity analysis: 2008, **134**, 65–77.

———, 2008b, An image-focusing semblance functional for velocity analysis: SEP-Report, **136**, 43–54.

De Vries, D. and A. J. Berkhout, 1984, Velocity analysis based on minimum entropy: Geophysics, **49**, 2132–2142.

Fomel, S., 2002, Applications of plane-wave destruction filters: Geophysics, **67**, 1946–1960.

Fomel, S., E. Landa, and M. T. Taner, 2007, Poststack velocity analysis by separation and imaging of seismic diffractions: Geophysics, **72**, U89–U94.

Hale, D., 2007, Local dip filtering with directional laplacians: CWP-Report, **567**.

Harlan, W. S., J. F. Claerbout, and F. Rocca, 1984, Signal/noise separation and velocity estimation: Geophysics, **49**, 1869–1880.

Landa, E., S. Fomel, and M. Reshef, 2008, Separation, imaging, and velocity analysis of seismic diffractions using migrated dip-angle gathers: SEG Technical Program Expanded Abstracts, **27**, 2176–2180.

Reshef, M., 2008, Interval velocity analysis in the dip-angle domain: Geophysics, **73**, VE353–VE360.

Reshef, M. and A. Rüger, 2008, Influence of structural dip angles on interval velocity analysis: Geophysics, **73**, U13–U18.

Sava, P., 2004, Migration and velocity analysis by wavefield extrapolation: PhD thesis, Stanford University.

Sava, P. C., 2003, Prestack residual migration in frequency domain: Geophysics, **68**, 634–640.

Sava, P. C., B. Biondi, and J. Etgen, 2005, Wave-equation migration velocity analysis by focusing diffractions and reflections: Geophysics, **70**, U19–U27.

Stinson, K., E. Crase, W.-K. Chan, and S. Levy, 2005, Optimized determination of migration velocities: Recorder, **30**, 5–6.

Wang, B., V. Dirks, P. Guillaume, F. Audebert, and D. Epili, 2006, A 3d subsalt tomography based on wave-equation migration-perturbation scans: Geophysics, **71**, E1–E6.